JOURNAL OF SPACECRAFT AND ROCKETS

Return of OSPREE: In Situ Spectroscopic Measurements During Atmospheric Reentry

Ashwin P. Rao,* Jack D. Crespo,† Paolo Valentini,‡ Vanessa J. Murray,§ and Erin I. Vaughan¶
U.S. Air Force Research Laboratory, Kirtland Air Force Base, New Mexico 87117
Zach S. Davis**
Space Dynamics Laboratory, Albuquerque, New Mexico 87106
and
Robert Alviani†† and Marat Kulakhmetov‡‡
Varda Space Industries, El Segundo, California 90245

https://doi.org/10.2514/1.A36508

Optical emission spectroscopy measurements of the reentry shock layer can provide invaluable information about the dynamic aerothermal chemistry during atmospheric reentry and yield critical data needed to improve fluid dynamics modeling of reentry systems. On 28 February 2025, the U.S. Air Force Research Laboratory successfully executed the Optical Sensing of Plasmas in the ReEntry Environment (OSPREE) experiment using Varda Space Industries' W-2 hypersonic test-bed vehicle, obtaining in situ shock-layer radiative emission measurements during reentry from an altitude of 105 km down through 50 km, encompassing a range of Mach numbers between 29.5 and 15.0. We present a summary of the reconstructed trajectory and the optical emission spectra obtained during flight, noting key emissions pointing to evolving shock-layer thermochemistry and interactions between the flowfield and vehicle thermal protection system. Temporal evolution of the spectral radiance of key molecules (CN, C_2, CH) and atoms (O, O^+, N, and H) is analyzed across the flight trajectory. Rotational and vibrational temperatures from spectral fits are computed to provide thermometric measurements of the shock layer over time.

Nomenclature

P_∞ = freestream pressure, Pa
Re = Reynolds number
T_r = rotational/rotranslational temperature, K
T_v = vibrational temperature, K
T_∞ = freestream temperature, K
t_{int} = spectrometer integration time, ms
v_∞ = freestream velocity, m/s
z = altitude, km
α = angle of attack, deg
α_T = total angle of attack, deg
β = side wind angle, deg
λ = wavelength, nm
ρ_∞ = freestream density, $\mathrm{kg/m^3}$
ϕ = total sideslip angle, deg
Kn = Knudsen number
χ_i = mole fraction of species i

I. Introduction

ATMOSPHERIC reentry vehicles traveling at near-orbital velocities create strong bow shocks that compress and heat the freestream air to temperatures in excess of 10,000 K. These bow shocks effectively convert the kinetic energy of incoming air molecules into thermal and internal energies. Consequently, the extremely energetic collisions between these molecules cause dissociation, ionization, and electronic excitation [1–5]. Furthermore, because the fluid advection, thermal excitation, and chemical reaction time constants at these conditions become comparable, these reentry flows also experience significant thermochemical nonequilibrium [6–8]. These thermochemical nonequilibrium flows are of great scientific interest due to the effects they can have on vehicle aerodynamics, aeroheating, and the ability to sense and communicate during reentry [9,10]. However, studying high-enthalpy nonequilibrium flows remains a challenge due to difficulty matching conditions in a laboratory setting and measuring data without obstructing the flow [11].

The high-enthalpy flow around a reentry vehicle generates a luminescent plasma that radiates across the ultraviolet (UV), visible (VIS), and near-infrared (NIR) parts of the electromagnetic spectrum [12]. Radiative emissions from the shock-heated air can be analyzed using optical emission spectroscopy (OES) to record emitted photons with high spectral resolution [13]. The transition features present in an emission spectrum can be matched to specific atoms and molecules, elucidating the chemical makeup of the shock layer as the vehicle reenters [14,15]. Direct comparisons of flight-test OES data to synthetic spectra generated from coupled fluid dynamics and radiative emission solvers can benchmark the accuracy of nonequilibrium chemistry models used in these computational methods and identify critical gaps in validation data needed to improve simulation fidelity [16,17]. Furthermore, spectral sensors do not perturb the flow and can be fielded with less risk than other external measurement probes. Historically, flowfield emissions have been collected with ex situ measurements using ground or airborne platforms, as seen with the Hayabusa, Hayabusa2, and Stardust planetary entry missions [18–21]. However, no high-resolution in situ OES measurements of a high-enthalpy shock layer made from within an atmospheric reentry spacecraft exist in the public domain. The European Space Agency developed an in situ UV/NIR OES payload for the EXPERT vehicle, but the test flight never occurred due to the loss of a launch opportunity [22]. The Kentucky Reentry Universal Payload System deployed a set of small reentry capsules from the Cygnus vehicle that contained Hamamatsu mini spectrometers embedded in the thermal protection system (TPS). The telemetry limitations of Iridium forced the spectral data to be collapsed into six color bins rather than being transmitted at full resolution [23]. To date, the best prior shock-layer OES data were collected on

---

Received 9 June 2025; accepted for publication 16 October 2025; published online Open Access 12 December 2025.

*Section Chief; ashwin.rao.1@us.af.mil. Young Professional AIAA.

†Associate Research Engineer. Member AIAA.

‡Senior Research Engineer. Senior Member AIAA.

§Experiments Lead.

¶Testbed Lead.

**Computational Aerospace Engineer. Senior Member AIAA.

††Aerodynamics Engineer. Member AIAA.

‡‡Head of Analysis and Hypersonics. Member AIAA.

the bow shock ultraviolet (BSUV) 1 and 2 sounding rocket flights in 1990 and 1991; this data set has been used extensively for hypersonic model validation. These flight experiments only reached 3.5 km/s (Mach 12) and 5.1 km/s (Mach 17) for BSUV-1 and BSUV-2, respectively [15,16,24]. Furthermore, these were sounding rocket experiments that do not fully replicate the aerothermodynamic conditions of atmospheric reentry systems. A comprehensive in situ spectral data set beyond the UV obtained in the high enthalpy environment at true reentry speeds (Mach 25+) would be of great benefit to the hypersonic and reentry modeling community, providing key temporally resolved shock-layer chemistry measurements from a unique line of sight without interference from surface heating emissions or atmospheric absorption.

On 28 February 2025, the U.S. Air Force Research Laboratory and Varda Space Industries successfully executed the Optical Sensing of Plasmas in the ReEntry Environment (OSPREE) experiment using Varda's W-2 hypersonic test-bed vehicle [25]. In situ OES data were obtained during atmospheric reentry from an altitude of 105 km down to 50 km, encompassing a Mach range between 29.5 and 15.0. Section II of this paper describes this mission with details of the W-2 vehicle geometry, reconstructed W-2 trajectory, and details of the OSPREE payload required for interested readers to anchor models to the presented data. Section III of this paper then presents key results and evolution of spectral emissions along the reentry trajectory. Important emission features are identified to include O (777 nm), O^+ (501–522 nm), N (740-748 nm), and H_α (656.3 nm) as well as the CN red and N_2 1st Positive systems (600-800 nm), CN violet (371-391 nm), C_2 Swan (500-517 nm), and CH A-X (426-433 nm). Section IV of this paper then uses the data in Sec. III to analyze temporal evolution of shock-layer thermochemistry, including species spectral radiance, key emission ratios, and rotational and vibrational temperatures determined from spectral fitting. We expect this paper to be a comprehensive, agnostic summary of the W-2 mission and spectral measurements collected by the OSPREE payload on this flight. The readers should contact the corresponding author if they require additional raw data collected on this flight. Future work will use this data to analyze and improve nonequilibrium direct simulation Monte Carlo (DMSC) and computational fluid dynamics (CFD) models.

II. Mission Overview

A. Launch, Reentry, and Recovery Operations

Varda's W-2 spacecraft containing OSPREE launched from Vandenberg Space Force Base, California, on SpaceX's Transporter 12 (Falcon 9) on 14 January 2025. It deployed at 500 km and entered a sun-synchronous orbit, where it remained for 6 weeks conducting microgravity pharmaceutical manufacturing. The OSPREE payload was dormant during this on-orbit period. Resistance temperature detectors monitored the payload's health and engaged heater pads to keep internal temperatures above −30°C. Deorbit operations began on 25 February 2025. The first two burns raised the vehicle apogee, lowered the perigee, and phased the vehicle with the landing site. The Koonibba Test Range in South Australia, operated by Southern Launch, was chosen as the landing and recovery site for the W-2 mission. The final deorbit burn took place on 27 February 2025 and placed the vehicle on a reentry trajectory with an approximate 4 deg flight-path angle.

On 27 February 2025, at 1401:54 hrs Coordinated Universal Time (UTC), the capsule separated from the satellite bus and continued a ballistic reentry. This separation time is used as the reference time ($t = 0$ s) for all analyses in this paper. The OSPREE payload powered on approximately 6 min after separation, synced with the vehicle flight computer timer 10 min after separation, and continued collecting data through 14 min after separation. The sync with the flight computer made it possible to align OSPREE measurements with the reconstructed flight data in subsequent sections. The OSPREE payload powered off a few minutes before parachute deployment to protect the embedded memory from data corruption issues caused by parachute snatch and landing shock loads. Figure 1 details the timing sequence of these key reentry mission events.

W-2 successfully deployed parachutes and touched down in South Australia at 1430:17 hrs UTC and was subsequently recovered the next morning. Terrestrial landing enabled the OSPREE payload to collect and store reentry spectra at high resolution; in contrast, previously mentioned flight experiments had to down-sample and upload the measurements via telemetry before the test vehicles were lost [15,16,24,26]. In addition to the OSPREE payload, the W-2 vehicle also carried a GoPro camera that recorded the entire reentry. This camera made it possible to compare the evolution of the one-dimensional spectra to two-dimensional images of the shock layer [27]. This test flight was also tracked by multiple ground and air platforms that will be discussed in future publications. A single long exposure of the capsule taken from the ground near Koonibba is shown in Fig. 2a, and an image of W-2 on the ground after flight is shown in Fig. 2b.

B. Spacecraft Design

The W-series vehicle was originally developed by Varda Space Industries to support manufacturing and recovery of microgravity payloads [28]. The vehicle has evolved into a dual-use hypersonic test bed for external customers to perform experimentation and technology maturation in the reentry environment; W-2 was the first flight under this hypersonic test-bed program. The technical details of the W-series reentry capsule and the sensor payload are described in

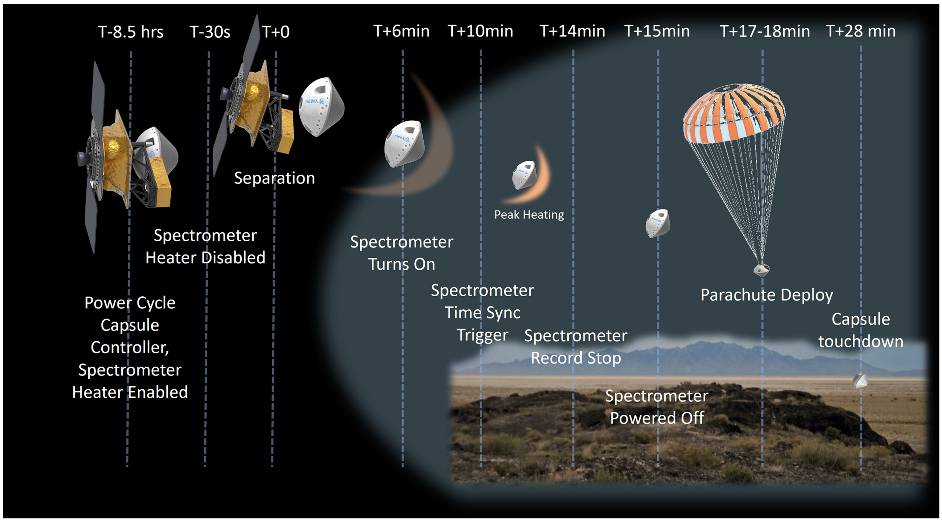

Fig. 1 **Sequence of critical mission operation events for the W-2 capsule and OSPREE payload.**

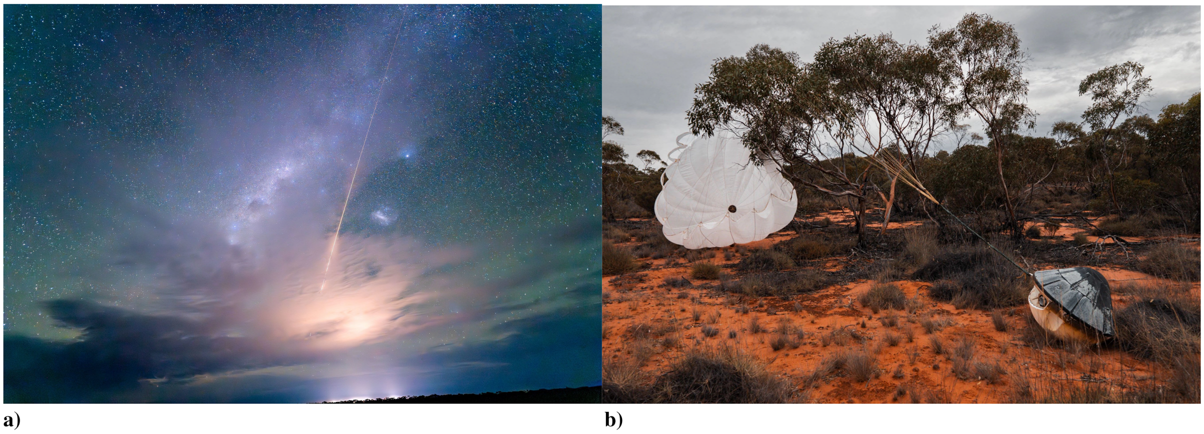

Fig. 2 Images of the W-2 reentry capsule highlighting. a) Long exposure of W-2 capsule streak across the South Australian desert and b) W-2 after landing at Koonibba Test Range.

great depth in a previous publication that presents the development, qualification, and premission simulations of OSPREE [25].

The simplified W-2 aeroshell geometry is presented in Fig. 3. The vehicle is a 45 deg sphere–cone with a hemispherical aft body. The capsule is 0.9 m in diameter ($D = 0.9$ m), and all of its supporting geometry is scaled to this dimension. The capsule has a 0.25D nose radius and an aft hemisphere centered at 0.32D. The capsule is mostly axisymmetric; however, it has three pockets on the aft body which are separated by 120 deg. The pockets can be modeled as extruded cylinders with a notch that are 0.1408D in diameter. The OSPREE collimating lens and the GoPro camera sit in two of these pockets. The former sits in the pocket aligned with the y axis, and the latter sits in the pocket rotated clockwise, while looking at the nose of the capsule. The dimensions in Fig. 3a are sufficient to fully define the simplified vehicle geometry for most CFD simulations. The reader should contact corresponding author Rao of this manuscript if they require additional details. The blue triangle in Fig. 3a denotes the view and line of sight of both the camera and OSPREE collimator.

The body coordinate system used to define vehicle dynamics and payload orientation is presented in Fig. 3b. In all subsequent plots, the x axis is defined out of the vehicle nose. The OSPREE collimator is oriented along the y axis and the GoPro camera is oriented along a vector that is rotated 120 deg about the x axis from the y axis. Reconstructed vehicle attitudes, in the next section, are defined via the angle of side wind β and angle of attack α. Because the velocities relevant to the OSPREE measurements are much higher than high-altitude winds, these angles also define the orientation of the vehicle nose relative to the flight-path vector. This orientation can be obtained by an α rotation around the y axis followed by a β rotation around the resultant z axis, as shown in Fig. 3b. A total angle of attack α_T is also defined as an angle between the velocity vector and the body centerline, while a roll angle ϕ is defined as a rotation around the x axis. The spectrometer is on the windward side when ϕ is positive and leeward side when it is negative.

The W-2 capsule flew with a conformal phenolic impregnated carbon ablator (C-PICA) TPS on the forebody and a minimally ablative backshell TPS. The C-PICA TPS is expected to inject carbon and hydrogen species into the shock layer via pyrolysis and ablation. These species produce strong signatures early in flight, while the air number density is still low. The present work does not provide a detailed material response or blowing rates for PICA; however, readers interested in studying how pyrolysis of PICA affects the chemistry and emissions in the shock layer are encouraged to obtain a copy of Fully Implicit Ablation and Thermal analysis program (FIAT) or Porous material Analysis TOolbox (PATO) [29,30]. Although some of the properties of PICA are restricted, researchers interested in publishing in the open literature can use the simplified PICA models found in Refs. [31–34]. For example, Park recommends treating the pyrolysis gas as a mixture of 37.5% C, 46.3% O, and 16.2% H. Furthermore, researchers focusing on the continuum part of the flight trajectory, at altitudes below 70 km, can largely ignore effects of ablation because emissions in this range are dominated by standard air chemistry.

The PICA tiles on the vehicles have two coating layers. PICA tiles with no coating are labeled *PICA*, tiles with just the first coating are labeled *PICA-A*, and tiles with both coatings are labeled *PICA-B*. Small amounts of room-temperature vulcanizing silicone (RTV) are also present in various areas of the outer mold line of the vehicle. This RTV chars in flight and injects impurities into the flow. There are two types of RTV used, labeled as *RTV-1* and *RTV-2* in this

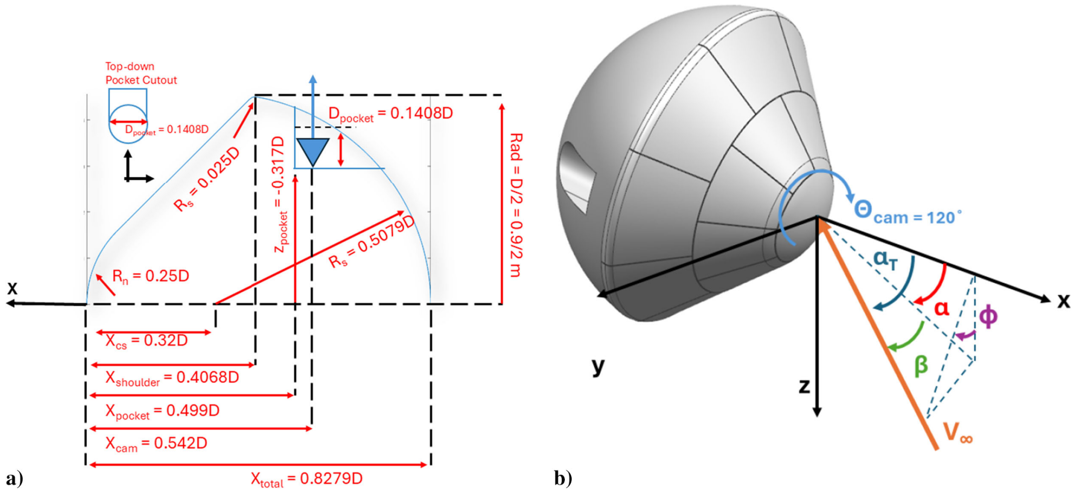

Fig. 3 Varda reentry capsule: a) geometry definition and b) coordinate system definition.

paper. To characterize potential spectral contamination, the team tested all TPS and RTV samples with a laser-induced breakdown spectroscopy (LIBS) technique. The results of these tests are presented in Figs. 4a and 4b. The Fe I 623 nm emission has been identified in RTV-2. The 589 nm Na doublet was identified in LIBS spectra taken from all other TPS samples. These Fe I and Na doublet signatures appear in the flight emission spectra and are discussed further in Sec. III. A more detailed analysis of PICA contamination on this flight is published in a separate journal that is currently under review.

C. Reconstructed Trajectory and Key Flight Parameters

In addition to the OSPREE payload, W-2 also contained a GPS receiver, an inertial measurement unit (IMU), a GoPro camera, and thermocouple sensors. The Photon Bus, which hosted the W-2 capsule in orbit, was equipped with an additional GPS and IMU, a star tracker, and other proprietary sensors to determine vehicle state while in orbit. Sensor data were fused together to reconstruct the reentry trajectory. The NASA software New Statistical Trajectory Estimation Program (NewSTEP) was used to build this reconstruction with guidance from Langley Research Center staff [35]. The flight reconstruction was then validated by simulating the camera view based on reconstructed attitudes, using the Exploration Visualization Environment (EVE) software, and comparing the video to the actual GoPro recording from the vehicle. This comparison is depicted in Fig. 5 at the 113 s postseparation point. The orientation of Earth horizon in both the true and simulated videos have a good match. The reader is encouraged to review the entire reentry flight video from Ref. [27].

Various properties of the reconstructed trajectory, relevant to the measurement range of the OSPREE payload, are presented in Figs. 6a–6e. The capsule-satellite bus separation point is used as the reference time in all flight reconstructions. Figure 6a shows the ground track the W-2 capsule took from separation to its final landing site at the Koonibba Test Range. The OSPREE spectrometer collected spectral signal from 669 to 781 s after separation. The vehicle altitude and velocity in this time interval are shown in Fig. 6b. The vehicle was able to maintain GPS lock for half of this flight duration. The altitude and velocity measured directly by the GPS are included as circles in this figure, while altitude and velocity reconstructed from IMU measurements are presented as solid lines. Reconstructed vehicle attitudes are presented via angle of attack α and angle of side wind β angles in Fig. 6c or alternatively via a total angle of attack α_T and sideslip angle ϕ in Figs. 6d and 6e. Note that the W-2 capsule is a statically and dynamically stable aeroshell that naturally orients into the flow as the dynamic pressure increases along the trajectory. At altitudes above 80 km, the vehicle's angle of attack (AOA) oscillated by as much as 40 deg while the vehicle was stabilizing. This AOA oscillation dropped to under 5 deg at altitudes below 80 km. The vehicle also picked up an engineered roll rate at 750 s, which kept angle of attack oscillations locked for the remainder of the flight. Because of this roll, the GoPro camera and the spectrometer are expected to see the same flow after the 750 s trajectory point. During the stabilization period, the spectrometer was exposed to varying amounts of the windward and leeward sides of the vehicle. Because OES measurements are affected by variations in plasma temperature [21,36] the spectral data are also affected by the AOA. Consequently, we advise conducting simulations of the vehicle using α_T, with the optical LOS extracted at the correct attitude.

The W-2 mission did not fly air data probes or measure freestream air properties in situ. Instead, air properties along the flown

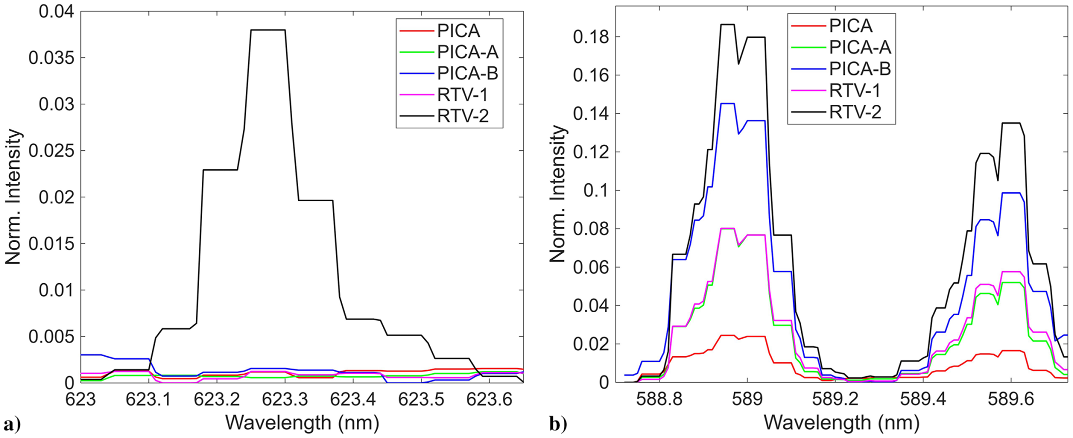

Fig. 4 Normalized LIBS spectra of W-2 TPS samples taken in a laboratory indicating a) Fe contamination in the RTV and b) presence of Na in every TPS material.

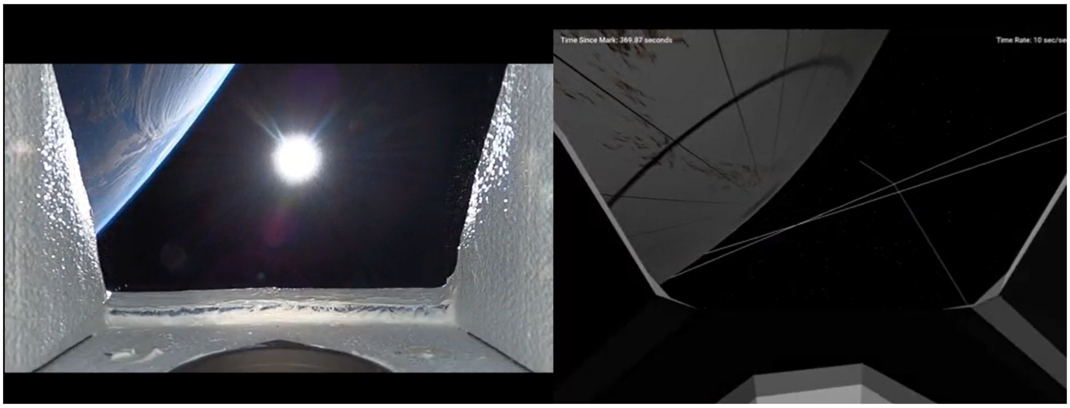

Fig. 5 Flight reconstruction is validated by comparing actual GoPro flight video (left) to simulated camera view from the reconstructed trajectory (right). The presented comparison is at 113 s after separation. GoPro flight video for the whole trajectory can be obtained from Ref. [27].

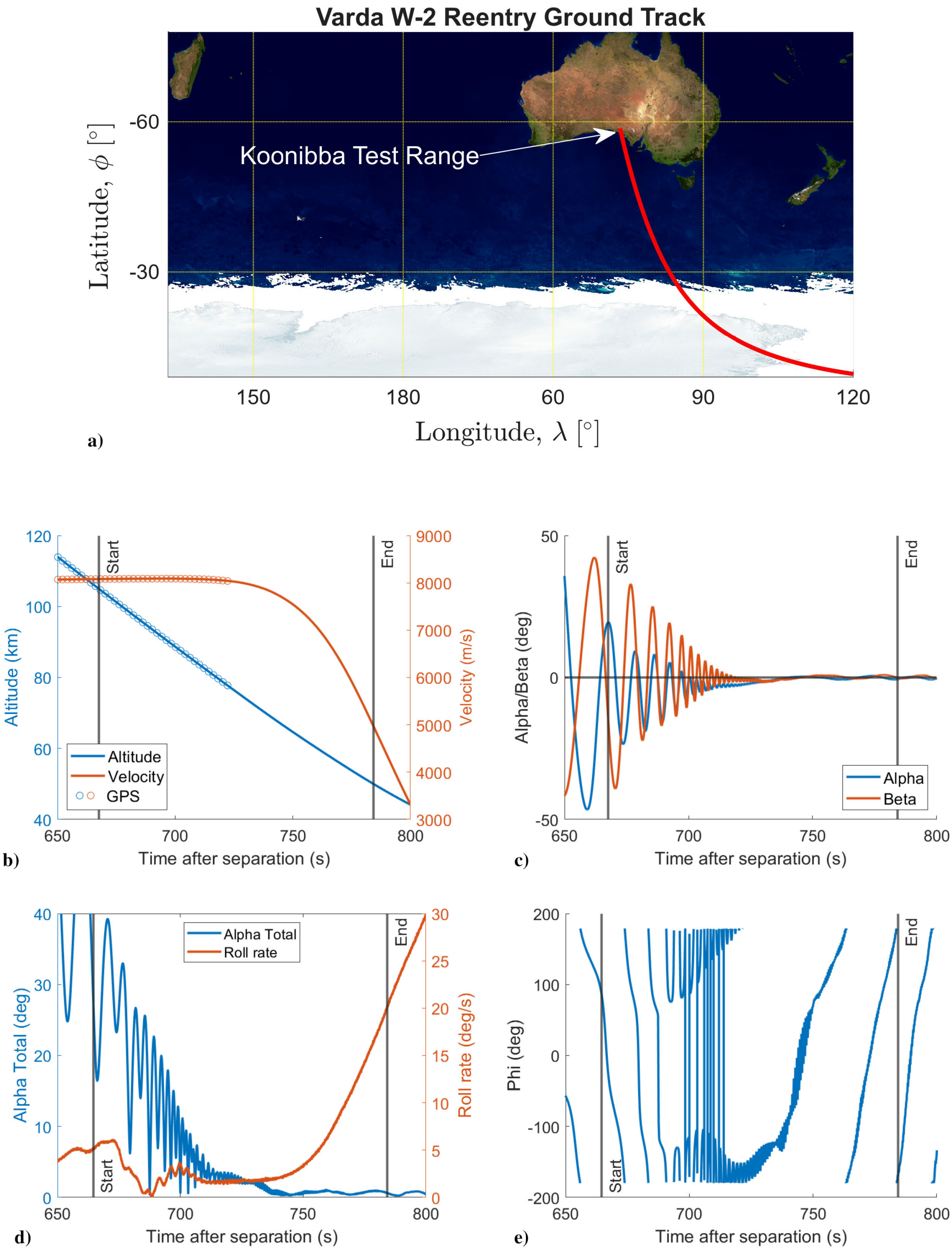

Fig. 6 W-2 trajectory reconstruction data detailing a) ground track of reentry into Koonibba, b) altitude and velocity, c) angles of attack α and side wind β, d) total angle of attack α_T, and e) sideslip angle ϕ during the OSPREE recording period.

trajectory were obtained via stitching together the Earth Global Reference Atmospheric Model (EarthGRAM), the Goddard Earth Observing System, Version 5 (GEOS-5) assimilation model, and day-of weather radiosonde data. EarthGRAM is a NASA atmospheric model that provides realistic, statistically based profiles of Earth's atmosphere for space mission and aerospace vehicle simulations [37]. The GEOS-5 model is an assimilation model that propagates atmospheric states corrected via worldwide atmospheric temperature, moisture, wind, and other measurements [38]. Both models are sensitive to time of flight, day of flight, and flown trajectories. Therefore, both models were sampled for the trajectory flown on W-2. The freestream atmospheric properties along this trajectory which are pertinent to the OSPREE payload are shown in Figs. 7a–7e. Note that the GEOS-5 model is expected to be more accurate but only extends up to 80 km altitudes. To accommodate for the entire trajectory, it is common to stitch together the GEOS-5 model, up to this altitude, into the EarthGRAM model.

To support subsequent analysis based on this report, six reference points are extracted from the reconstructed trajectory and presented in Table 1 along with all freestream properties required to conduct fluid dynamics simulations of the vehicle at these locations. These six reference points are tied to the presented spectral analysis. It should be noted that the presented mass fractions for each point do not add to unity. The remainder is accounted for by trace gases in the atmosphere, mainly argon, helium, and CO_2. The small freestream amounts of these trace gases have negligible effects on flowfield chemistry and are omitted in the majority of air chemistry models used in CFD/DSMC codes.

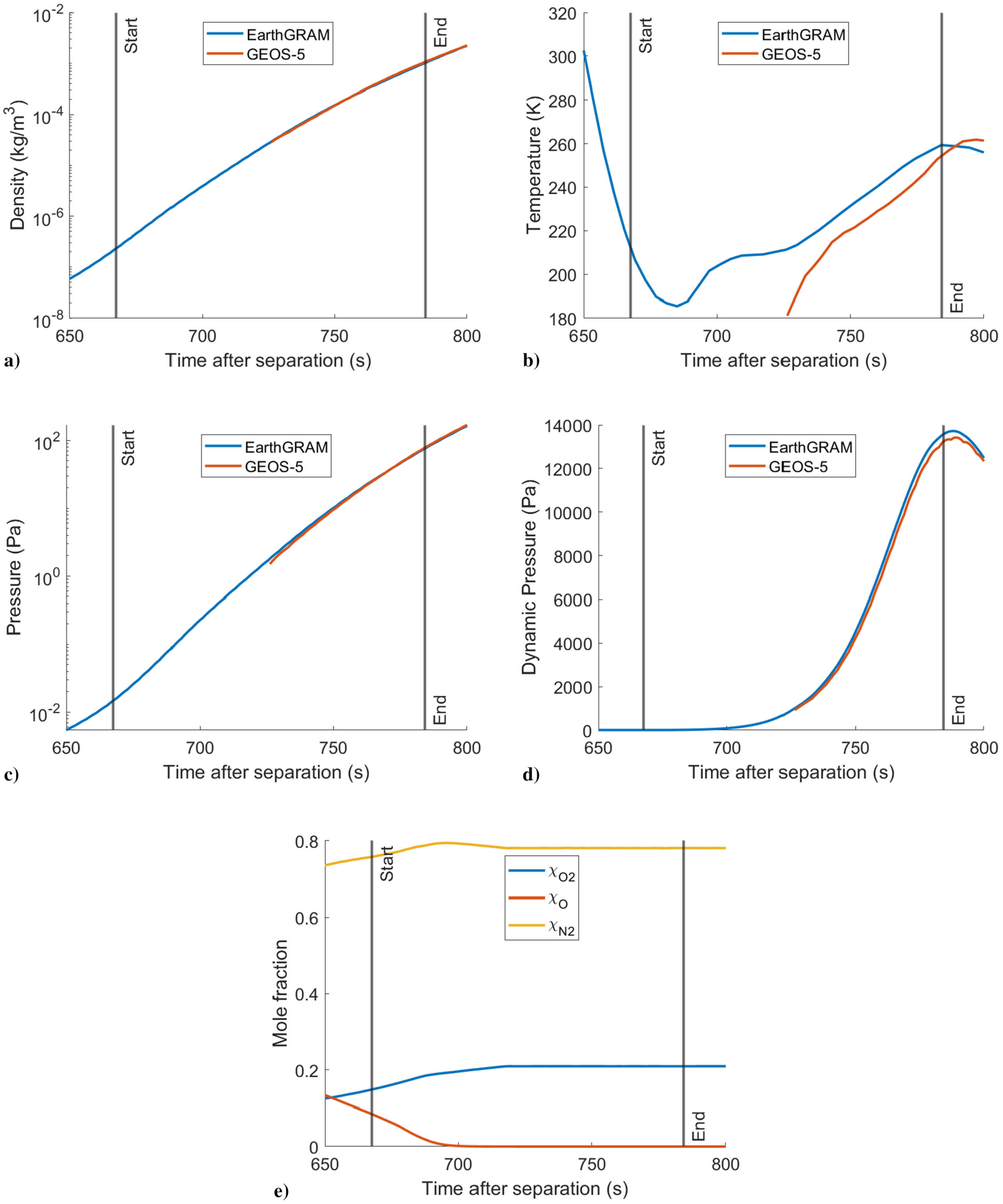

Fig. 7 Freestream a) density, b) temperature, c) pressure, d) dynamic pressure, and e) species mole fraction variation over reconstructed trajectory.

Table 1 Six reference trajectory points for the W-2 reentry with corresponding altitude, Mach, freestream velocity, pressure, density, temperature, Reynolds and Knudsen numbers, and species mole fractions [38]

Time, s	z, km	Mach	v_∞, m/s	P_∞, Pa	ρ_∞, kg/m^3	T_∞, K	Re	Kn	χ_{O_2}	χ_{O}	χ_{N_2}	χ_{N}
669	104.3	28.0	8080	0.016	2.60e-07	207.64	139	0.2633	0.151	0.081	0.759	0
689	94.2	29.5	8086	0.084	1.54e-06	187.68	473	0.0414	0.186	0.015	0.79	0
709	84.3	29.2	8066	0.468	7.81e-06	208.41	3639	0.0081	0.203	0.0002	0.787	0
735	70.6	25.4	7838	4.1	6.50e-05	219.43	33380	0.0010	0.209	0	0.781	0
755	61.4	22.7	7194	16.1	2.36e-04	237.87	104295	0.0003	0.209	0	0.781	0
781	50.5	15.1	5184	71.3	9.61e-04	258.71	278108	0.0001	0.209	0	0.781	0

D. OSPREE Payload Design

OSPREE comprises nearly entirely of commercial-off-the-shelf (COTS) hardware modified for spaceflight, as shown in Fig. 8a. The aft body of the capsule, which houses the aft pockets and windows, is removed in this image; however, the collimator on the left side of this figure sits directly behind one of the aft dome windows. The OSPREE payload uses a COTS Ocean Optics HR2 spectrometer which records emission spectra between 340 and 800 nm with a resolution of $\Delta\lambda = 0.23$ nm at full-width-half-maximum. Spectrometer control and data acquisition (DAQ) are conducted with a Raspberry Pi Compute Module 4 (RPi CM4), using the OceanDirect software development kit and Python RPi GPIO functions to trigger the sensor, set exposure time, and save recorded spectra into CSV files on the CM4 embedded multimedia card (EMMC). The HR2 charge -coupled device (CCD) was programmed to cycle continuously between integration times of 25, 50, 100, and 250 ms during flight, saving 10 spectra at each integration time in a single CSV file before cycling to the next value. This was done to protect against over- or undersaturating the spectral measurements in flight. Optical collection is conducted using a 0.25 in. diameter vacuum rated collimating lens (Accuglass 112689) positioned behind one of the optical windows, with a line of sight (LOS) directly perpendicular to the separation pocket out into the expansion region above the capsule's shoulder, annotated in Fig. 8b. This collimator has an effective light spot of 0.16 in., an effective focal length of 0.472 in., and a back focal length of 0.418 in. The collimator collects light within the effective light spot along the annotated LOS into the shock layer. A high-temperature, vacuum-rated InF_3 optical fiber (Thorlabs MFV1L1), with core diameter of 100 μm, coupled the collimator to the spectrometer for light transmission to the sensor. The payload assembly was subjected to random vibration, thermal vacuum, and electromagnetic interference qualification testing per the SpaceX Falcon 9 Rideshare Payload User's Guide. During payload assembly and qualification, an HgAr calibration pen lamp recording was implemented to ensure nominal performance of the sensor and to detect potential changes to the internal optics [25]. This process was repeated upon recovery of the payload during data extraction to assess changes from nominal configuration that occurred during reentry. No major differences between pre- and postflight calibration spectra were found from this analysis, indicating the spectrometer's internal optical components survived in their standard configuration from launch through reentry. A second calibration using a tungsten-halogen lamp (Thorlabs SLS201L) with a color temperature of 2796 K was conducted with the final assembly to obtain a system conversion factor for the spectrometer at each integration time, allowing for the conversion of the detector response to spectral radiance.

III. Overview of Spectral Data and Major Emission Features

Postflight GPS data reconstruction and correlation with OSPREE .csv file timestamps indicated the payload was powered on at 275 km and recorded data down to 35 km. Within this range, a spectral signal greater than the dark current noise was detected starting at 105 km down through 50 km. The signal interval compared to the total recording period is shown in Fig. 9a. Velocity measurements from GPS data at these altitudes indicate the spectral data obtained by OSPREE covers a range of Mach numbers from Mach 29.5 to Mach 15. To our knowledge, there are no publicly available in situ OES measurements from an orbital reentry at these speeds, making this a historically important data set for the future of hypersonics and reentry systems. Figure 9b shows six selected spectra taken from 105 to 50 km using a 250 ms integration time. The drastic rise in signal intensity and the appearance of multiple atomic and molecular emission features is evident between 104.3 km (red) and 70.6 km (magenta). Signal then decreases below detectable limits around 50 km in this wavelength range. This data demonstrate evolving aerothermal chemistry during the descent, which can be further investigated by identifying major emission

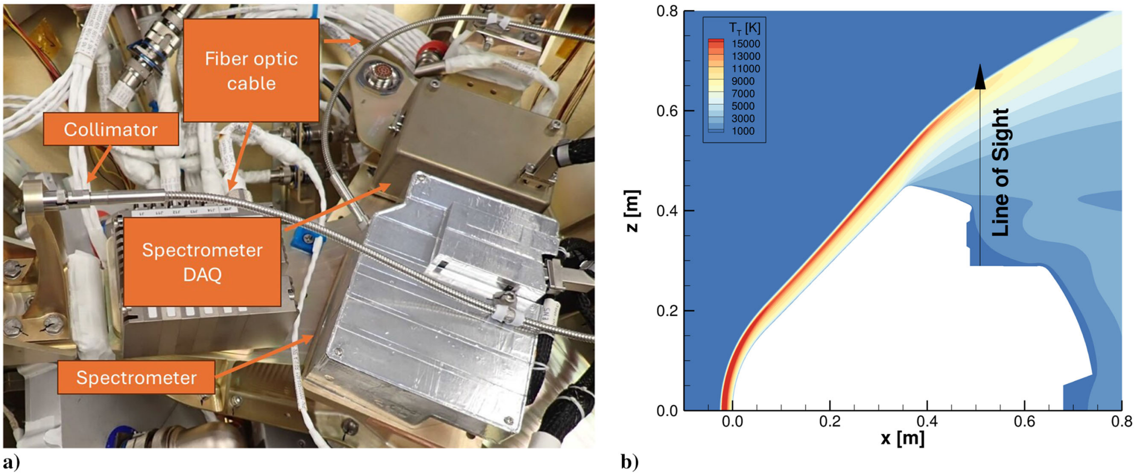

Fig. 8 OSPREE payload configuration details illustrating. a) OSPREE components on payload mounting deck integrated within W-2 [25] and b) line of sight of optical measurement into shock layer.

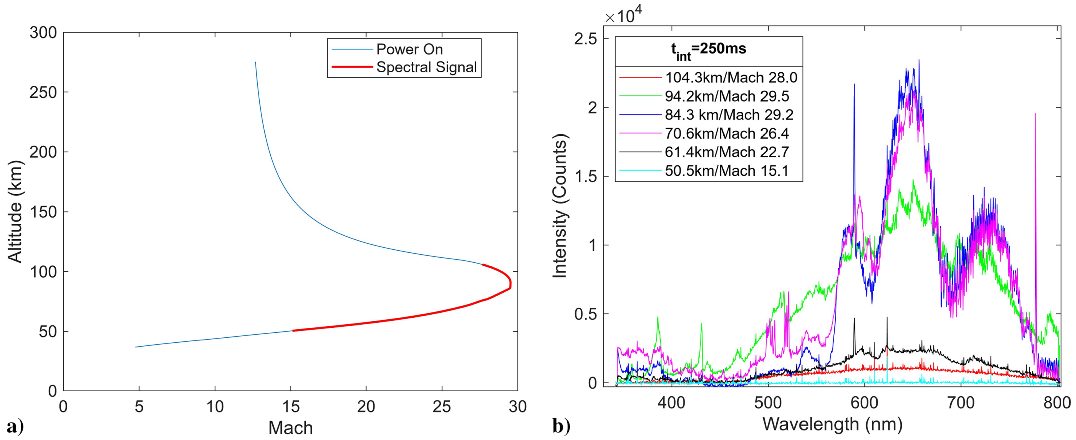

Fig. 9 OSPREE data summary illustrating. a) W-2 trajectory altitude vs Mach number (blue line) during OSPREE collection period, highlighting interval of spectral signal between 105 and 50 km (red line), and b) evolution of spectra from 105 to 50 km taken with 250 ms exposure time.

features and analyzing their temporal evolution during the reentry. We present selected spectra across the signal altitude range and identify major emission species at those trajectory points to better understand the evolving shock-layer chemistry.

Spectral signal was first detected at 667 s postseparation around 103 km, at which point shock-layer radiation was noticeable in the VIS NIR. Figures 10a and 10b provide a GoPro video frame of the shock layer and spectra taken at 669 s with corresponding spectra taken during this interval. As plasma forms around the vehicle, the spectrometer detects the thermal emissions from the heated gas along with atomic emissions from the PICA coatings on the forebody. Clear molecular emission features are not yet prevalent at this time. However, the distinct rise in intensity above the background/dark current levels indicates that the spectrometer was sensitive enough to detect these thermal emissions, even in rarefied flow conditions. Figure 10b also presents spectra collected with 50, 100, and 250 ms integration times. The longer integrations increased the signal intensity without oversaturating or modifying the signal. Thus, even though data exist for all integration time intervals at all trajectory points, only the 250 ms integration times will be presented in the remainder of this subsection.

A significant change in the spectrum occurs as the capsule reaches Mach 29.5 and descends below 100 km, shown in Figs. 11a and 11b. Multiple strong and well-resolved emissions from various carbon species are seen, notably the CN violet $\Delta v = 0$, CH (A-X), C_2 Swan $\Delta v = 0$, and CN red band from 600–800 nm. This suggests the continued production of C-PICA pyrolysis and ablation products being introduced into the flow as well as various reactions between C_2 and N_2 forming CN, which is known to be a strong radiator in its violet ($B^2\Sigma^+$—$A^2\Sigma^+$) and red ($A^2\Pi$—$X^2\Sigma$) emission bands. Previous mass spectrometry studies of pyrolysis product formation from resistively heated PICA indicate that the molar yield is dominated by H_2, CH_4, H_2O, and CO, along with appreciable quantities of phenol, cresol, and dimethyl phenol [39]. Further chemical reactions between these products as well as air molecules in the shock layer, may form CN, CH, C_2, C_3, NH, OH, CO, C_2H, and H_2 [34,40]. Although not all of these species are seen in the data, they are likely present in the shock layer and either 1) radiating in the UV or IR outside OSPREE's range or 2) being occluded or hidden under the radiation of the stronger species annotated in Fig. 11b. The presence of the radiative emissions of these molecules indicates that the heat shield, likely the nose tile at the stagnation point, reached high enough temperatures for the C-PICA to begin pyrolyzing and introducing these gases into the flowfield. Additionally, the shock layer is sufficiently hot to rovibrationally excite these molecules such that these emission features are present, even at 98 km in rarefied conditions. Another interesting observation from the spectrum is the presence of the sodium doublet (Na D_1/D_2) at 589 nm as well as a strong atomic emission line of Fe at 623.3 nm. The Na emission stems from elemental contaminants in the TPS material or its coatings, as shown in Sec. II. Na is a pervasive contaminant in many materials and can be introduced into TPS at various stages in the manufacturing process as well as by human contact. The Na doublet persists as a strong emission feature due to

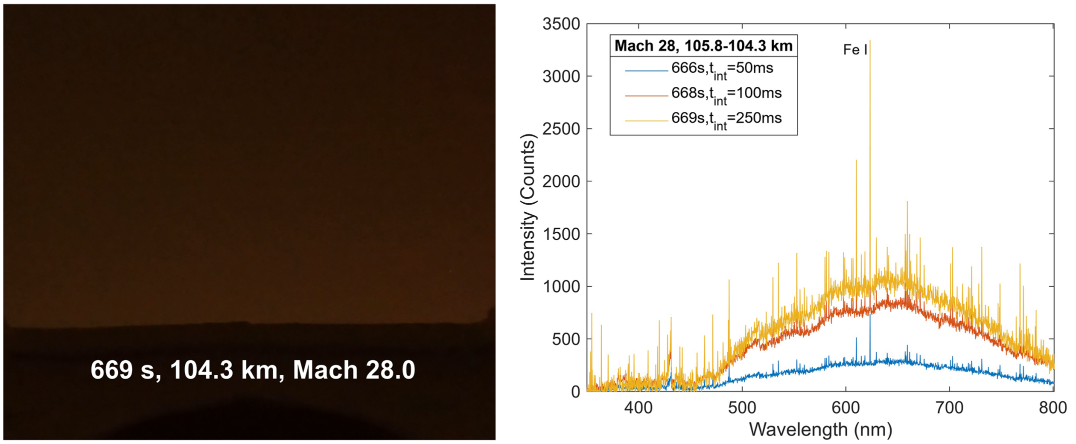

a) b)

Fig. 10 Shock layer LOS data showing a) video frame of shock layer at 669 s (104.3 km) showing start of shock-layer emission and b) beginning of noticeable spectral signal between 106–104 km.

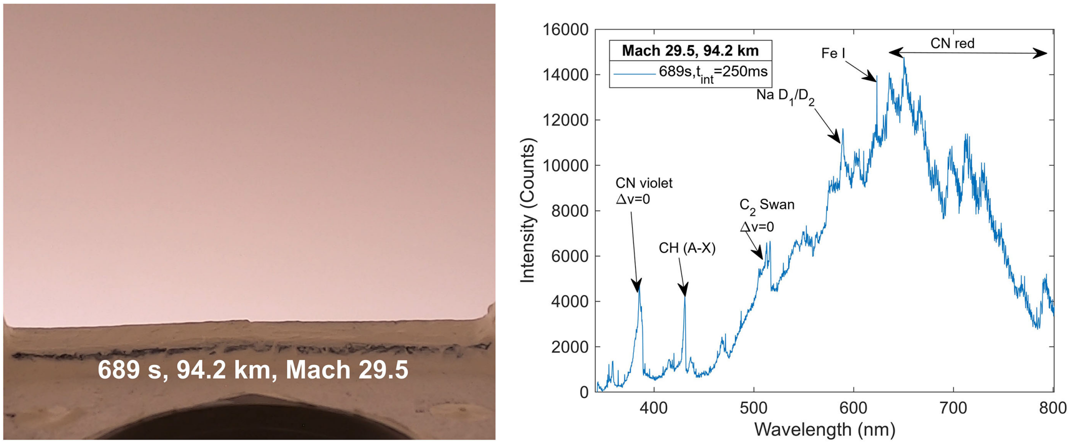

a) b)

Fig. 11 Shock layer LOS data showing: a) video frame of shock layer at 689 s (94.2 km) showing increased visible emission radiance and b) spectrum at 94.2 km with multiple strong emissions of TPS pyrolysis products and atomic impurities labeled.

sodium being a strong oscillator. The appearance of sodium in this data set will be of great interest to those in the hypersonics community studying the effects of alkali contaminants in shock-layer chemistry. These elements are easily ionizable through impact ionization reactions (e.g., $Na + O \rightarrow Na^+ + O^-$ or $Na + e^- \rightarrow Na^+ + e^- + e^-$ [41]) and can increase the electron density of the plasma if present in high enough quantities. The source of Fe in the spectra was identified as the RTV silicone used in the gaps between capsule forebody tiles. The emission intensity behavior of these elemental contaminants observed during reentry provides highly valuable data for enhancing the fidelity of material response models coupled to aerothermal solvers to compute shock-layer/TPS interaction chemistry.

As the capsule transitions from the rarefied to continuum flow regime between 87 to 70 km, dissociation of air molecules and excitation of free atoms occur in the shock layer. O_2 dissociation and O excitation begin to occur at 87.7 km and increase as the capsule enters continuum flow conditions and slows down due to the denser air. Figures 12a and 12b show a drastic change in visible shock-layer emission color along with the the strong emission of N_2, O, O^+, and Na in the spectrum. Notably, the 600–800 nm range is dominated by the N_2 1st. Positive ($B^3\Pi_g$-$A^3\Sigma_u^+$) system rather than CN red, due to the increasing density of the air. The hydrogen Balmer α transition is seen at 656.3 nm, indicating breakdown of the phenolic resin within the PICA into its atomic constituents. Figure 12c highlights the emission intensity behavior of the O 777 nm emission between 87.7 and 70.6 km. The 777 nm emission has been used extensively for ground tracking and spectral observation of reentry systems, namely, Hayabusa and Hayabusa2 [18,20], assessing the temporal evolution of shock-layer emissions, benchmarking computed spectral radiance from fluid dynamics modeling [42], and estimating shock heated gas temperature [21]. The 777 nm emission appears around 702 s (87.7 km) after separation, rising in intensity as the capsule slows from its peak Mach number. The temporal evolution of the radiance of this emission will be critical in assessing the accuracy of radiative emission models of the W-2 shock layer and better understanding the chemical reactions driving O_2 dissociation and O excitation. O^+ multiplet emissions are seen between 500 and 522 nm, indicating ionization reactions occurring in the shock layer. Comparing the relative emission radiances of O^+ to O over time will also provide a valuable metric of the accuracy of the ionization chemistry models in existing fluid dynamics solvers. Similarly, Fig. 12d highlights three atomic nitrogen emissions between 740 and 748 nm. These were also observed by Johnston during the Hayabusa2 airborne observation [42] and suggest dissociation reactions involving N_2 as well as CN occurring in the shock layer during this period.

As the capsule descends further into the continuum flow regime, the emission spectrum is dominated by the N_2 1st Positive system between 600 and 800 nm. Figures 13a and 13b show TPS ablation/spallation visible in the shock layer at 750 s (63.7 km) as well as the diminishing spectral intensity between 737 (69.6) and 757 s (60.9 km). By 757 s postseparation, the N_2 features and the O 777 nm emission are below detectable limits because the spectrum consists mostly of thermal emissions from the shock heated gas as well as residual elemental impurities (Na/Fe). The decrease in signal intensity and loss of major atomic and molecular emission features during this period indicate cooling of the gas in the flowfield and the diminishing of the plasma. To further probe shock-layer chemistry evolution during this period, we convert the measured spectra to units of spectral radiance and examine the temporal evolution of key emitters during flight.

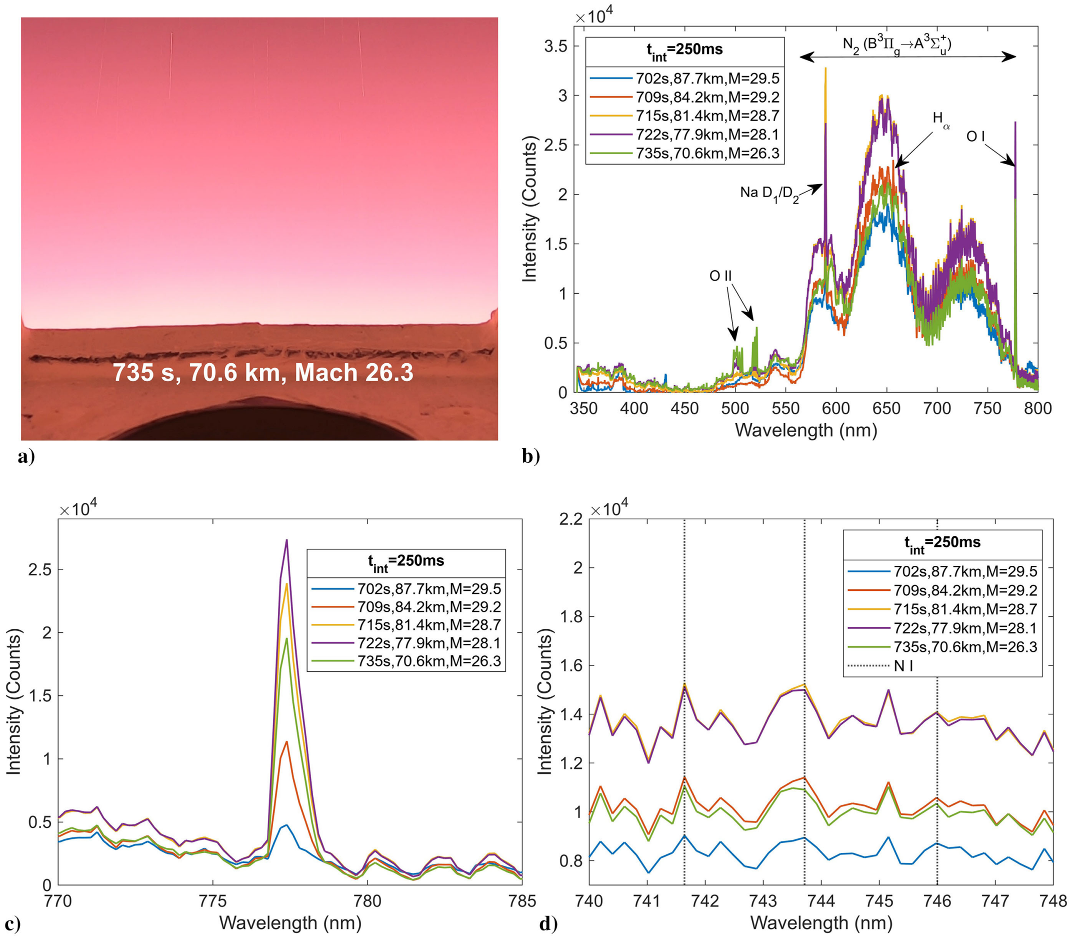

Fig. 12 Shock layer LOS data showing a) video frame of shock layer at 735 s (70.6 km) along with b) spectra between 702 s (87.7 km) and 735 s (70.6 km) with strong O, O^+, H, Na, and N_2 emissions and focus on specific emissions of c) O and d) N in this altitude range.

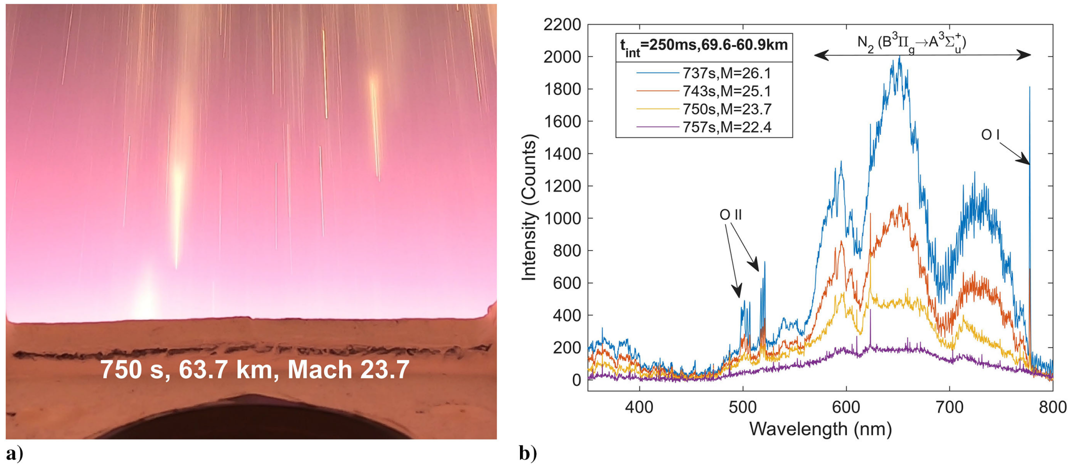

Fig. 13 Shock layer LOS data showing a) video frame of shock layer at 750 s (63.7 km) showing spallation debris from TPS along with b) spectra between 737 s (69.6 km) and 757 s (60.9 km) showing strong emission from O, O^+, and the N_2 1st Positive system. Signal diminishes as the capsule slows.

IV. Analysis of Time Evolving Shock-Layer Thermochemistry

A. Temporal Evolution of Species Spectral Radiance

Measured spectra were converted to spectral radiance with a system conversion factor calculated before launch using a blackbody calibration source [43]. This conversion factor converted the data to intensity units agnostic of the detector exposure time for proper analysis of temporal emission evolution and comparison to simulation data. Table 2 lists the specific emissions analyzed in this section and their corresponding species, wavelengths, and energy transition levels provided by NIST [44].

We begin with an analysis of the radiance of O, O^+, and N using the O 777 nm emission, O^+ multiplet emissions between 504 and 521 nm, and the three minor N emissions between 740 and 748 nm exhibiting $3p^4S°/3p^4D°/3p^4P° \rightarrow 3s^4P$ transitions. Figure 14 displays the temporal evolution of the O, O^+, and N radiance from 650 to 790 s after separation. The vertical lines mark the altitudes and Mach numbers at the time steps corresponding to the appearance, approximate peak, and diminishing intensity of these atomic lines. N radiance begins to gradually rise at 680 s, whereas the 745 nm emission begins to manifest in the spectrum among the increased thermal emissions from the start of the heat pulse. The radiance of N continues a gradual increase until its peak value of 5.42×10^{-3} W/cm^2/sr/μm at 717 s. In contrast, O radiance begins rising at 700 s and exhibits a rapid increase to its peak value of 1.43×10^{-2} W/cm^2/sr/μm at 725 s, nearly three times higher than the peak radiance of N. The drastic difference in radiance increase between these two atomic species indicates higher prevalence of O formation in the shock layer compared to N formation. Additionally, the difference in bond energies between N_2 (946 kJ/mol) and O_2 (498 kJ/mol) likely contributes to difference in the observed radiance. O^+ radiance remains several orders of magnitude lower than O radiance through the measurement period. The initial peak in O^+ radiance at 687 s (98.2 km) of 1.14×10^{-3} W/cm^2/sr/μm in rarefied flow conditions could be driven by charge exchange reactions with pyrolysis products (e.g., $CO^+ + O \rightleftharpoons CO + O^+$) [42] or electron bombardment of O. After decreasing to a local minimum at 707 s, O^+ radiance begins to rise again to a maximum of 1.42×10^{-3} W/cm^2/sr/μm at 737 s (75.4 km). The 12 s delay between the peaks of O and O^+ indicate a dependence on initial O_2 dissociation reactions forming O required for the ionization and subsequent excitation of O^+ to occur. The radiance of all atomic species decreases starting at 725 s (62.7 km) as shock-layer radiation subsides across the spectral range. The radiative emission intensities of these species are largely governed by both species number densities and excited-state populations. In a nonequilibrium plasma, excited-state populations are governed by rate coefficients describing processes such as collisional excitation, radiative decay, and electron impact processes. Thus, while O and N might be present along the LOS at similar number densities, collisional-radiative processes in the shock layer appear to drive higher excited-state populations of O. Furthermore, the bond energy difference between O_2 (5.2 eV) and N_2 (9.8 eV) would also lead to higher concentrations of O being formed in the shock layer. Similarly, O^+ concentrations in the shock layer are several orders of magnitude below that of O [25] along the LOS, helping explain the nearly two orders of magnitude difference in measured radiance between these two species.

Table 2 Spectral ranges and associated species examined in this work to analyze temporal evolution of shock-layer chemistry [44]

Species	λ range, nm	λ_{peak}, nm	Energy levels (j–i)
CN	371–391	385.4	B–X
CH	426–433	431.3	A–X
C_2	500–517	516.2	Π_g-Π_u
H_α	655–658	656	6–4
N	740–748	743.6	10–4
O	775–780	777.6	6–4
O^+	504–521	517.6	4–2

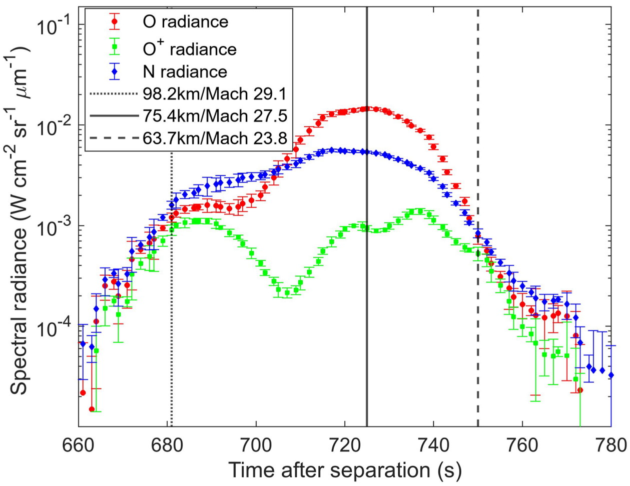

Fig. 14 Spectral radiance of O, O^+, and N vs time, with vertical lines denoting altitudes and Mach numbers across the range in which these emissions were present.

In addition to prevalent atomic species from the air, we analyze the temporal evolution of various species formed by the interaction between pyrolyzing/ablating TPS and the shock-heated air. Figure 15 tracks the temporal evolution of the peak radiance of the CN violet

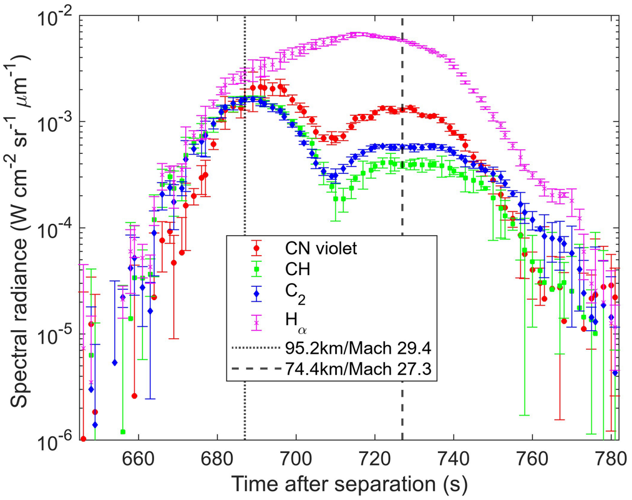

Fig. 15 **Spectral radiance of CN violet, CH, C_2, and H emission peaks vs time, corresponding to changes in interactions between pyrolysis/ablation products and shock-heated air.**

$\Delta v = 0$, CH, and C_2 Swan $\Delta v = 0$ molecular features in addition to H_α. The radiance of all three molecules begins rising around 670 s, with CN slightly lagging C_2 and CH. C_2 and CH radiance peaks at 687 s, while CN peaks slightly later at 692 s. All three species exhibit a peak radiance from $1.5\text{–}3.0 \times 10^{-3}$ W/cm^2/sr/μm. The lag in the initial rise and peak of CN may stem from intermediate reactions between pyrolysis products and N_2 or N, which occur to form CN, whereas C_2 and CH can form directly from the pyrolyzing phenolic or carbon fibers, as well as interactions between shock heated air and charred PICA. Furthermore, the H radiance rises sharply to 3.13×10^{-3} W/cm^2/sr/μm, indicating pyrolysis and rapid breakdown of the phenolic resin within the heat shield.

The radiance of all three molecules drops sharply between 688 and 710 s to a local minimum and then begins rising again to a secondary peak at approximately 727 s. The initial decrease in radiance of these molecules corresponds to the time interval where the O spectral radiance rises the fastest. This behavior could be indicative of a shift in the chemical reactions occurring during this period dominantly driving higher levels of O production and excitation. During this period, the radiance of H continues to rise uniformly at a slower rate to a peak value of 6.73×10^{-3} W/cm^2/sr/μm, indicating continued breakdown of the phenolic resin and production of H in the shock layer. As the rise of O radiance approaches its inflection point near 710 s, the radiance of the carbon molecular species also rises, with the secondary peak of CN/CH/C_2 aligning with the peak O spectral radiance. An interesting observation reflected in the secondary peak of Fig. 15 is the larger difference in the peak radiances of the three species compared to the primary peak at 687s. CN presents strongest at 1.81×10^{-3} W/cm^2/sr/μm, followed by C_2 and CH at 5.79×10^{-4} and 4.08×10^{-4} W/cm^2/sr/μm, respectively. The difference in species radiance at this point in the trajectory is likely driven by two factors: 1) the density of the air and 2) prior decomposition/pyrolysis of the heat shield and phenolic at higher altitudes. The increase in the air density between 95.2 and 74.4 km leads to a much larger number density of N_2 present in the shock layer, which could, in turn, favor air chemistry producing CN relative to CH or C_2. Second, because pyrolysis began early in the descent at 98 km, it is likely that more phenolic resin near the TPS surface was already depleted by 74 km, thus introducing less CH and C_2 into the shock layer. This is supported by the data as the radiance of H begins to decrease around 715 s. Toward the end of the period of recorded emissions, CN and CH radiances decrease and reach steady state by 750 s, while H and C_2 persist at a lower level out to 770 s, likely due to emissions from TPS spallation debris in the flowfield. These measurements tied to TPS/shock-layer interaction will be of great use in baselining performance of ablation and material response solvers coupled to fluid dynamics codes and building on prior computational studies modeling the response of PICA in hypersonic environments [34,40,42,45–48].

Finally, experimental measurements of PICA pyrolysis [33] have revealed that H_2O is a dominant product of the temperature-dependent phenolic pyrolysis. H_2O injected in the hot, partially dissociated shock-layer gas is then likely to form OH either via direct dissociation with other molecular or atomic constituents (e.g., $H_2O + M \leftrightarrow OH + O + M$) or via exchange processes with other atomic species (e.g., $C + H_2O \leftrightarrow CH + OH$) [49]. Subsequent OH dissociation is also a likely process which might reduce its concentration and therefore cause a negligibly small emission. Incorporation of these additional gas/phase chemical mechanisms involving OH in computational studies is thus required.

B. Species Intensity Ratios

Analyzing the radiant emission intensity ratios of certain observable species can further elucidate how shock-layer chemistry evolves during reentry and help ascertain how aerochemistry changes during flight.

Figures 16a and 16b shows the time evolution of the ratios of O/N as well as O^+/O. Figure 16a reflects the dominance of O compared to N between 710 and 750 s. This behavior indicates that O_2 dissociation is more prevalent than that of N_2 in this range between 84 to 64 km, and the shock-layer conditions in this regime favor both O production and excitation. Similarly, O ionization reactions can be assessed using Fig. 16b; the data indicate a higher presence of ionized oxygen between 666 (105) and 695 s (90 km), followed by a rapid reduction in O^+ through 710 s (84 km) and a secondary gradual rise in ionization through 750 s (64 km). Emission intensity ratios from spectra computed using fluid dynamics solutions can be compared to these experimental intensity ratios across the trajectory to assess the accuracy of reaction rates used in the chemistry models

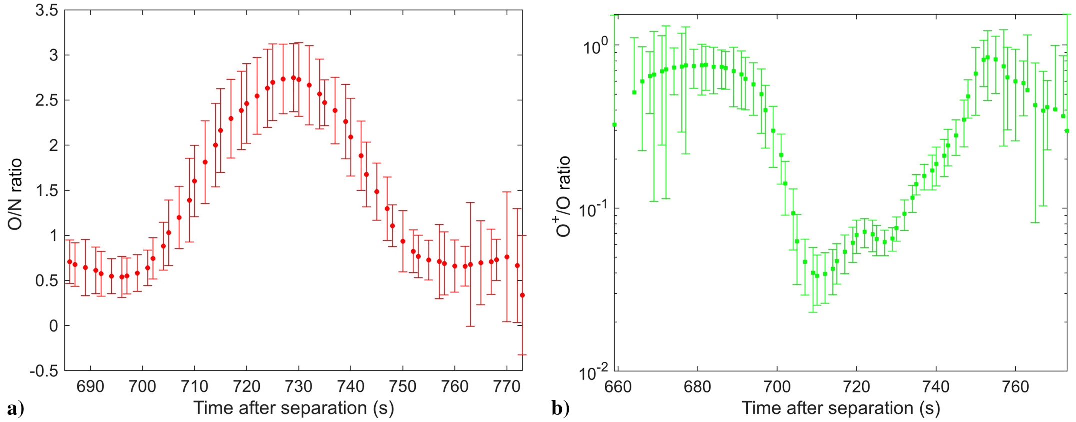

Fig. 16 **Radiance ratios during reentry of a) O/N and b) O^+/O.**

employed by these solvers. This work is in progress and will be presented in a future study.

C. Shock-Layer Thermometric Measurements via Spectral Fitting

The Specair program [50] was used to perform nonequilibrium, multispecies fits for several of the averaged spectra (in units of spectral radiance) ranging from 686 to 747 s after separation. Fitting was conducted using a global optimization routine to provide an equilibrium fit temperature to a combination of the N_2 1st Positive, CN red, and O 777 nm emissions. Translational/rotational T_r and vibrational/electronic T_v temperatures were equilibrated to follow the simulation methodology using the Park two-temperature air chemistry model employed in Ref. [25], and a separate fitting optimization routine was used to adjust the two temperatures until residuals between the fit and experimental data were minimized. This two-temperature approximation is sufficient for most nonequilibrium CFD models; future work will use a four-temperature nonequilibrium fit to this data set. Effects of instrument broadening on the spectrum were calculated using the slit function for the OSPREE system, which was measured with a HeNe laser before integration. Figure 17 provides an example of the Specair two-temperature fit to the recorded radiance at 89.2 km as well as the calculated T_r and T_v. Figure 18 illustrates the temporal evolution of T_r and T_v between an altitude range of 95.7 to 65.5 km, where recorded spectral features had enough resolution to be fit by the Specair routine. Because of the nature of the LOS measurement and collimator properties discussed in Sec. II, it was assumed that the hotter, more radiant portion of the shock layer along the LOS dominates the recorded spectral emission. Thus, the temperatures determined through the fitting routine are most representative of the portion of the LOS closest to the shock itself.

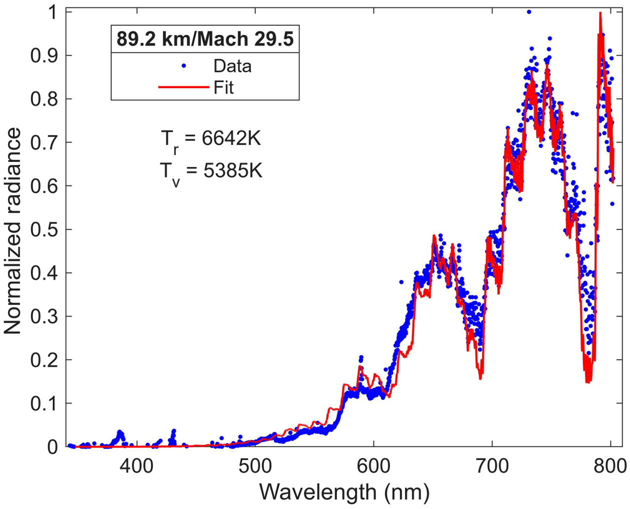

Fig. 17 Comparison of measured spectral radiance (blue) to Specair nonequilibrium fit (red) at 89.2 km.

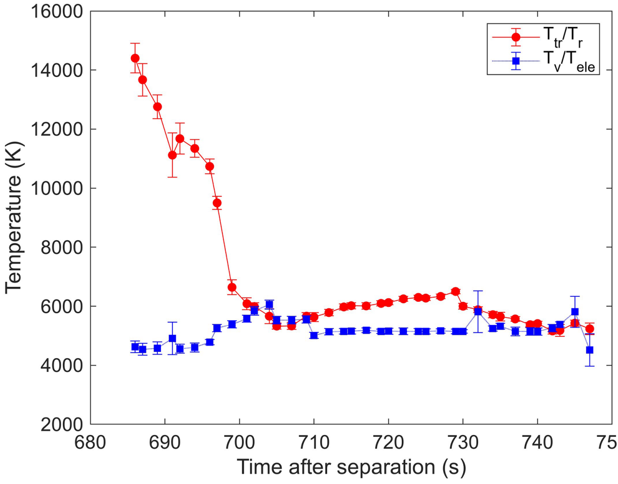

Fig. 18 Temporal evolution of rotranslational (red) and vibrational (blue) temperatures determined by Specair fits to flight data.

Significant thermal nonequilibrium is seen at higher altitudes corresponding to rarefied flow conditions. The calculated T_r starts at a high of 14,400 K at 686 s (95.7 km/Mach 29.3) and drops drastically to 5663 K by 704 s (86.7 km/Mach 29.5). In this same interval, T_v exhibits a steady rise from 4627 to 6057 K. This time interval corresponds to the first peak and subsequent drop of the $CN/C_2/CH$ emissions in Fig. 15, indicating that high T_r drives the excitation and emission of pyrolysis products at high altitudes, despite the low density of the flow. At these lower temperatures, carbon-based material also ablates through oxidation, introducing species like CO into the shock layer. These species can undergo further reactions to produce some of the observed molecules from this data set, such as CN. From 705 to 729 s (86.2 km/Mach 29.5–73.9 km/Mach 27.2), T_v decreases slightly and remains relatively static at an average value of around 5150 K, while T_r rises gradually to 6500 K. This period coincides with the main rise and peak of the O 777 nm radiance (Fig. 14) as well as the secondary increase in the radiance of pyrolysis reaction products (Fig. 15). Additionally, the sustained shock-layer heating of the TPS up to this period drives sublimation of the carbon char, leading to the production of heavier species such as C_2, also reflected in Fig. 15. Assuming rotranslational equilibrium, the increase in T_r during this period would drive increased population of atomic excited states as well as rotationally excited ($\Delta V = 0$) molecular energy states, as reflected in the data. T_r then drops to 5100 K between 730 (72.9 km/Mach 27) and 747 s (65.5 km/Mach 24.5) in continuum flow conditions, bringing the two temperatures closer to equilibrium as the observed radiance of all species of interest declines. Past this point, temperatures could not be calculated from the measured radiance due to loss of feature resolution as shock-layer emission subsided, leading to large uncertainties in the fitted temperature. The temperature data extracted from this 1 min window during reentry elucidates observed trends in the time-evolving radiance of key species and helps quantify the degree of thermal nonequilibrium in the flowfield. Additionally, these measurements will provide valuable comparison data to assess the accuracy of LOS temperatures calculated by fluid dynamics solvers of this vehicle in the future.

V. Conclusions

The atmospheric reentry and recovery of W-2 and successful execution of the OSPREE flight experiment has yielded an invaluable data set for the hypersonics enterprise. A comprehensive set of emission spectra detailing time-evolving shock-layer chemistry across a 50 km altitude range covering high-hypersonic through reentry speeds was obtained, providing historic OES measurements in these flight regimes. Time evolution of key chemical species such as C_2, CN, CH, H, N_2, N, O, and O^+ were analyzed throughout the trajectory to assess changes in shock layer chemistry during the vehicle's descent. Emission features were computationally fit to determine rotational and vibrational temperatures, which indicated the presence of strong thermal nonequilibrium at high altitudes as well as a correlation between rotational temperature and emission radiance. Our preliminary analysis in this manuscript intends to convey high-level results and conclusions from the mission. A greater body of work tied to these data will be conducted in future studies directly comparing the experimental results to synthetic spectra generated from nonequilibrium fluid dynamics models. The authors hope this data set will be useful to the community and help to improve existing computational tools and advance the state of the art of modeling and simulation capabilities.

Acknowledgments

The authors acknowledge the efforts of NASA Langley Research Center for their aid in the W-2 trajectory reconstruction, as well as the Strategic and Military Space group at Space Dynamics Lab for engineering/testing the payload and providing recovery operations support. The team also extends their gratitude and appreciation to the Koonibba Community Aboriginal Corporation, Southern Launch, and the Australian Space Agency for their support and partnership in this historic reentry mission. The views expressed are those of the author(s) and do not necessarily reflect the official policy or position of the Department of the Air Force, the Department of Defense, or the U.S. government. This work is categorized as distribution unlimited and approved for public release, AFRL Public Affairs Release #AFRL-2025-2671.

Acknowledgments

This research was partially funded by a U.S. Air Force Research Laboratory Edison grant as well as a Lab Task Grant from the Air Force Office of Scientific Research (grant number RVCOR005, Amanda Chou), supporting the scientific objectives of a funded effort between Varda and U.S. Air Force Research Laboratory under SPACEWERX STRATFI contract FA-9453-23-C-A035. Engineering and qualification efforts were funded under contract FA-9453-18-D-0042 between U.S. Air Force Research Laboratory and the Utah State University Space Dynamics Laboratory.

References

[1] Petrova, T. B., Petrov, G. M., and Peñano, J. R., “Transport Properties of High Mach Number Hypersonic Air Plasmas,” *Plasma Sources Science and Technology*, Vol. 33, No. 11, 2024, Paper 115008. https://doi.org/10.1088/1361-6595/ad8ef1

[2] Anderson, J. D., “Hypersonic and High-Temperature Gas Dynamics,” *AIAA Education Series*, 2nd ed., AIAA, Reston, VA, 2006, pp. 449–458, Chap. 6.

[3] Kulakhmetov, M. F., “Upscaling Ab-Initio Chemistry Models to Non-Equilibrium Flow Simulations,” Ph.D. Thesis, Purdue Univ., West Lafayette, IN, 2016.

[4] Valentini, P., Zhang, C., and Schwartzentruber, T. E., “Molecular Dynamics Simulation of Rotational Relaxation in Nitrogen: Implications for Rotational Collision Number Models,” *Physics of Fluids*, Vol. 24, No. 10, 2012. https://doi.org/10.1063/1.4757119

[5] Candler, G. V., “Rate Effects in Hypersonic Flows,” *Annual Review of Fluid Mechanics*, Vol. 51, No. 1, 2019, pp. 379–402.

[6] Kulakhmetov, M., Gallis, M., and Alexeenko, A., “Ab Initio-Informed Maximum Entropy Modeling of Rovibrational Relaxation and State-Specific Dissociation with Application to the O_2 + O System,” *Journal of Chemical Physics*, Vol. 144, No. 17, 2016. https://doi.org/10.1063/1.4947590

[7] Panesi, M., Munafò, A., Magin, T., and Jaffe, R., “Nonequilibrium Shock-Heated Nitrogen Flows Using a Rovibrational State-to-State Method,” *Physical Review E*, Vol. 90, No. 1, 2014, Paper 013009. https://doi.org/10.1103/PhysRevE.90.013009

[8] Andrienko, D. A., and Boyd, I. D., “Kinetic Models of Oxygen Thermochemistry Based on Quasi-Classical Trajectory Analysis,” *Journal of Thermophysics and Heat Transfer*, Vol. 32, No. 4, 2018, pp. 904–916. https://doi.org/10.2514/1.T4968

[9] Bertin, J. J., and Cummings, R. M., “Critical Hypersonic Aerothermodynamic Phenomena,” *Annual Review of Fluid Mechanics*, Vol. 38, No. 1, 2006, pp. 129–157. https://doi.org/10.1146/annurev.fluid.38.050304.092041

[10] Starkey, R. P., “Hypersonic Vehicle Telemetry Blackout Analysis,” *Journal of Spacecraft and Rockets*, Vol. 52, No. 2, 2015, pp. 426–438. https://doi.org/10.2514/1.A32051

[11] Gu, S., and Olivier, H., “Capabilities and Limitations of Existing Hypersonic Facilities,” *Progress in Aerospace Sciences*, Vol. 113, March 2020, Paper 100607. https://doi.org/10.1016/j.paerosci.2020.100607

[12] Brandis, A. M., Johnston, C. O., and Cruden, B. A., “Nonequilibrium Radiation for Earth Entry,” AIAA Paper 2016-3690, June 2016. https://doi.org/10.2514/6.2016-3690

[13] Plumadore, A. D., Satija, A., Radhakrishna, V., Goldenstein, C. S., Chern, M., Goyne, C. P., Dedic, C. E., and Lucht, R. P., “Development of a Flight-Ready Optical Emission Spectroscopy Sensor for Hypersonic Flow,” *AIAA SCITECH 2023 Forum*, AIAA Paper 2023-1374, 2023. https://doi.org/10.2514/6.2023-1374

[14] Bose, D., and Candler, G. V., “Advanced Model of Nitric Oxide Formation in Hypersonic Flows,” *Journal of Thermophysics and Heat Transfer*, Vol. 12, No. 2, 1998, pp. 214–222. https://doi.org/10.2514/2.6324

[15] Erdman, P. W., Zipf, E. C., Espy, P., Howlett, C. L., Levin, D. A., Collins, R. J., and Candler, G. V., “Measurements of Ultraviolet Radiation from a 5-Km/s Bow Shock,” *Journal of Thermophysics and Heat Transfer*, Vol. 8, No. 3, 1994, pp. 441–446. https://doi.org/10.2514/3.562

[16] Boyd, I., Phillips, W., Levin, D., Boyd, I., Phillips, W., and Levin, D., “Sensitivity Studies for Prediction of Ultra-Violet Radiation in Nonequilibrium Hypersonic Bow-Shock Waves,” *35th Aerospace Sciences Meeting and Exhibit*, AIAA Paper 1997-0131, 1997. https://doi.org/10.2514/6.1997-131

[17] Levin, D., Candler, G., Collins, R., Erdman, P., Zipf, E., Espy, P., and Howlett, C., “Comparison of Theory with Experiment for the Bow Shock Ultraviolet Rocket Flight,” *Journal of Thermophysics and Heat Transfer*, Vol. 7, No. 1, 1993, pp. 30–36. https://doi.org/10.2514/3.11565

[18] Winter, M., and Herdrich, G., “Spectroscopic Observation of the STARDUST Re-Entry in the Near UV,” *39th AIAA Thermophysics Conference*, AIAA Paper 2007-4050, 2007. https://doi.org/10.2514/6.2007-4050

[19] Löhle, S., and Jenniskens, P., “High-Resolution Spectroscopy of the Hayabusa Reentry Using a Fabry–Perot Interferometer,” *Journal of Spacecraft and Rockets*, Vol. 51, No. 6, 2014, pp. 1986–1993. https://doi.org/10.2514/1.A32480

[20] Zander, F., Buttsworth, D. R., Birch, B., Noller, L., Wright, D., James, C. M., Thompson, M., Apirana, S., Leis, J., Lobsey, C., et al., “Australian Rapid-Response Airborne Observation of the Hayabusa2 Reentry,” *Journal of Spacecraft and Rockets*, Vol. 58, No. 6, 2021, pp. 1915–1919. https://doi.org/10.2514/1.A35062

[21] Birch, B., Zander, F., Buttsworth, D., Noller, L., and Payne, A., “Hayabusa2 Capsule Reentry: Visible and Near-IR Emission Spectroscopy from the Australian Airborne Observation,” *AIAA Aviation 2022 Forum*, AIAA Paper 2022-3736, 2022. https://doi.org/10.2514/6.2022-3736

[22] Lein, S., Reimer, T., Stubicar, K., Deuble, F., Auweter-Kurtz, M., Herdrich, G., and Winter, M., “Development of the Re-Entry Spectrometer RESPECT for the ESA Capsule EXPERT,” *Acta Astronautica*, Vol. 64, No. 4, 2009, pp. 416–426. https://doi.org/10.1016/j.actaastro.2008.07.024

[23] Ruffner, M. P., Ford, K. F., Craig, L. M., Tacchi, B. D., Schmidt, J. D., Poovathingal, S. J., Smith, W. T., and Martin, A., “Overview of the Hypersonic Test Flight KREPE-2,” *AIAA Aviation Forum and ASCEND*, AIAA Paper 2024-3561, 2024. https://doi.org/10.2514/6.2024-3561

[24] Erdman, P. W., Zipf, E. C., Espy, P., Howlett, C., Levin, D. A., Loda, R., Collins, R. J., and Candler, G. V., “Flight Measurements of Low-Velocity Bow Shock Ultraviolet Radiation,” *Journal of Thermophysics and Heat Transfer*, Vol. 7, No. 1, 1993, pp. 37–41. https://doi.org/10.2514/3.11566

[25] Rao, A. P., Crespo, J. D., Valentini, P., Taylor, J. B., Murray, V. J., Vaughan, E. I., Alviani, R., and Kulakhmetov, M., “Developing the OSPREE Payload for Spectroscopic Measurements of a Mach 25+ Plasma Sheath,” *Journal of Spacecraft and Rockets*, Vol. 62, No. 5, 2025, pp. 1–10. https://doi.org/10.2514/1.A36325

[26] Schmidt, J. D., Ruffner, M. P., Nichols, J. T., Rowe, I. S., Nolin, R. D., Ford, K. F., Smith, W. T., and Martin, A., “Kentucky Re-Entry Universal Payload System (KRUPS): Overview of Hypersonic Re-Entry Flight,” *AIAA SciTech 2023 Forum*, AIAA Paper 2023-0206, 2023. https://doi.org/10.2514/6.2023-0206

[27] Varda, “W-2 Reentry: Capsule View,” 2025, https://www.youtube.com/watch?v=XwQ6ib5SkMQ&t=12s.

[28] Bauser, H. C., Smith, P. A., Parent, S. D., Chan, L. R., Bhavsar, A. S., Condon, K. H., McCalip, A., Croom, J. M., Purcell, D. K., Bogdanowich-Knipp, S. J., et al., “Return of the Ritonavir: A Study on the Stability of Pharmaceuticals Processed in Orbit,” *ChemRxiv*, 2024. https://doi.org/10.26434/chemrxiv-2024-vb20g-v3

[29] Chen, Y.-K., and Milos, F. S., “Ablation and Thermal Response Program for Spacecraft Heatshield Analysis,” *Journal of Spacecraft and Rockets*, Vol. 36, No. 3, 1999, pp. 475–483. https://doi.org/10.2514/2.3469

[30] Omidy, A. D., Panerai, F., Martin, A., Lachaud, J. R., Cozmuta, I., and Mansour, N. N., “Code-to-Code Comparison, and Material Response

Modeling of Stardust and Msl Using Pato and Fiat," NASA CR 2015-218960, 2015.

[31] Park, C., "Calculation of Stagnation-Point Heating Rates Associated with Stardust Vehicle," *Journal of Spacecraft and Rockets*, Vol. 44, No. 1, 2007, pp. 24–32.
https://doi.org/10.2514/1.15745

[32] Covington, M., Heinemann, J., Goldstein, H., Chen, Y.-K., Terrazas-Salinas, I., Balboni, J., Olejniczak, J., and Martinez, E., "Erratum on Performance of a Low Density Ablative Heat Shield Material," *Journal of Spacecraft and Rockets*, Vol. 45, No. 4, 2008, pp. 854–864.
https://doi.org/10.2514/1.38249

[33] Bessire, B. K., Lahankar, S. A., and Minton, T. K., "Pyrolysis of Phenolic Impregnated Carbon Ablator (PICA)," *ACS Applied Materials & Interfaces*, Vol. 7, No. 3, 2015, pp. 1383–1395.
https://doi.org/10.1021/am507816f

[34] Winter, M., Butler, B., Danehy, P. M., Splinter, S., Diao, Z., Panerai, F., Martin, A., and Bailey, S., "Characterization of Ablation Product Radiation Signatures of Pica and Fiberform," *46th AIAA Thermophysics Conference*, AIAA Paper 2016-3233, 2016.
https://doi.org/10.2514/6.2016-3233

[35] Deshmukh, R. G., and Karlgaard, C. D., "Mars Exploration Rovers EDL Trajectory and Atmosphere Reconstruction Using NewSTEP," NASA TM 20210015330, 2021.

[36] Rao, A. P., Nawar, N., and Annesley, C. J., "Time-Resolved Diagnostic Measurements of Sub-Atmospheric Laser-Induced Air Plasmas Using the O, 777 nm Emission," *Optics Continuum*, Vol. 3, No. 2, 2024, pp. 187–199.
https://doi.org/10.1364/OPTCON.511770

[37] White, P. W., and Hoffman, J., "Earth Global Reference Atmospheric Model (Earth-GRAM): User Guide," NASA TM 20210022157, 2021, https://ntrs.nasa.gov/api/citations/20210022157/downloads/Earth-GRAM%20User%20Guide_1.pdf.

[38] Rienecker, M. M., Suarez, M., Todling, R., Bacmeister, J., Takacs, L., Liu, H.-C., Gu, W., Sienkiewicz, M., Koster, R., Gelaro, R., et al., "The GEOS-5 Data Assimilation System-Documentation of Versions 5.0. 1, 5.1. 0, and 5.2. 0," NASA TM 2008-104606, Vol. 17, 2008.

[39] Bessire, B. K., and Minton, T. K., "Decomposition of Phenolic Impregnated Carbon Ablator (PICA) as a Function of Temperature and Heating Rate," *ACS Applied Materials & Interfaces*, Vol. 9, No. 25, 2017, pp. 21,422–21,437.
https://doi.org/10.1021/acsami.7b03919

[40] Johnston, C. O., Gnoffo, P. A., and Sutton, K., "Influence of Ablation on Radiative Heating for Earth Entry," *Journal of Spacecraft and Rockets*, Vol. 46, No. 3, 2009, pp. 481–491.
https://doi.org/10.2514/1.40290

[41] Bortner, M. H., "The Chemical Kinetics of Sodium in Re-Entry," Tech. Rept. 64SD810, General Electric CO Philadelphia PA Missile and Space Div, 1964.

[42] Johnston, C. O., "Comparison Between Hayabusa 2 Spectral Measurements and Simulations," *AIAA AVIATION 2022 Forum*, AIAA Paper 2022-3799, 2022.
https://doi.org/10.2514/6.2022-3799

[43] Kulakhmetov, M. F., Alviani, R., Rao, A., Murray, V., Taylor, J. B., Seik, J., and Vaughan, E., "Optimizing Optical Emission Measurements on the Varda Hypersonic Testbed Vehicle," *AIAA Aviation Forum and ASCEND*, AIAA Paper 2024-4560, 2024.
https://doi.org/10.2514/6.2024-4560

[44] Ralchenko, Y., "NIST Atomic Spectra Database," *Memorie della Società Astronomica Italiana Supplement*, Vol. 8, 2005, p. 96.
https://doi.org/10.18434/T4W30F

[45] Martin, A., and Boyd, I. D., "Strongly Coupled Computation of Material Response and Nonequilibrium Flow for Hypersonic Ablation," *Journal of Spacecraft and Rockets*, Vol. 52, No. 1, 2015, pp. 89–104.
https://doi.org/10.2514/1.A32847

[46] Meurisse, J. B., Chatzigeorgis, G. B., Diaz, P. V., Bessire, B. K., Panerai, F., and Mansour, N. N., "Equilibrium Model for the Ablation Response of Silicone-Coated PICA," *International Journal of Heat and Mass Transfer*, Vol. 201, Oct. 2023, Paper 123523.
https://doi.org/10.1016/j.ijheatmasstransfer.2022.123523

[47] Langston, J. H., Wong, C., Diaz, N., Stefani, F., Salita, M., and Koo, J. H., "Validation of Ablation Model of Pica Using Fully Implicit Ablation and Thermal Response Program," *55th AIAA Aerospace Sciences Meeting*, AIAA Paper 2017-0896, 2017.
https://doi.org/10.2514/6.2017-0896

[48] Torres-Herrador, F., Meurisse, J. B., Panerai, F., Blondeau, J., Lachaud, J., Bessire, B. K., Magin, T. E., and Mansour, N. N., "A High Heating Rate Pyrolysis Model for the Phenolic Impregnated Carbon Ablator (PICA) Based on Mass Spectroscopy Experiments," *Journal of Analytical and Applied Pyrolysis*, Vol. 141, May 2019, Paper 104625.
https://doi.org/10.1016/j.jaap.2019.05.014

[49] Fujita, K., Yamada, T., and Ishii, N., "Impacts of Ablation Gas Kinetics on Hyperbolic Entry Radiative Heating," *44th AIAA Aerospace Sciences Meeting and Exhibit*, AIAA Paper 2006-1185, 2006.
https://doi.org/10.2514/6.2006-1185

[50] SpectralFit S.A.S, *Specair User Manual*, Ver. 3.0, 2025, http://www.specair-radiation.net/manual.php.

I. Leyva
Associate Editor